Journal of Alloys and Compounds 556 (2013) 102–108

Contents lists available at SciVerse ScienceDirect

Journal of Alloys and Compounds

journal homepage: www.elsevier.com/locate/jalcom

Controllable synthesis and optical properties of nano-CeO_2 via a facile hydrothermal route

Fanming Meng [a,b,*], Leini Wang [a], Jingbiao Cui [c]

[a] School of Physics and Materials Science, Anhui University, Hefei 230039, PR China
[b] Key Laboratory of Materials Modification by Laser, Ion and Electron Beams, Dalian University of Technology, Ministry of Education, Dalian 116024, PR China
[c] Department of Physics and Astronomy, University of Arkansas at Little Rock, Little Rock, AR 72204, USA

ARTICLE INFO

Article history:
Received 31 October 2012
Received in revised form 18 December 2012
Accepted 19 December 2012
Available online 29 December 2012

Keywords:
Nanostructures
Electron microscopy
X-ray photo-emission spectroscopy
Optical properties

ABSTRACT

Morphology control of CeO_2 nanostructures was achieved by using ethanol/water mixtures with varied volume ratios from 0:1 to 1:0 in a facile hydrothermal process with $CeCl_3{\cdot}7H_2O$ as cerium source and $N_2H_4{\cdot}H_2O$ as mineralizer. It was found that the increase of ethanol/water ratio resulted in the morphology change from thin nanorods to short-thick nanorods, and then to nanoparticles, which is mainly attributed to the influences of hydrocarbon chains, dielectric constant, and viscosity of the solution on the thermodynamics of the reaction system and kinetics of nucleation. Various characterization techniques have been used to study the CeO_2 nanostructures, including XRD, XPS, SEM, HRTEM, Raman, and PL spectra. Photoluminescence spectra of the CeO_2 nanoparticals exhibited an unique UV–violet–blue emission which is likely associated with the defect states existing extensively between Ce 4f and O 2p bands, better crystallinity of the sample, and higher concentration of Ce^{3+} ions in sample.

1. Introduction

Nanostructured functional materials have attracted much research interest due to their remarkable size-, shape-, or surface-dependent physical and chemical properties [1]. Ceria (CeO_2), one of the most important functional rare earth oxides, is a promising material for various applications in catalysts [2], fuel cells [3], oxygen sensors [4], magnetic materials [5], ultraviolet blocks [6], and optical materials [7] due to its oxygen storage capacity via facile Ce^{4+}/Ce^{3+} redox cycles, high mechanical strength, and unique optical properties. It is well known that the functionality of CeO_2 nanomaterials strongly depends on the morphology and size of the nanocrystals. Recent reports showed that low-dimensional CeO_2 possesses remarkable properties compared with its bulk counterparty. For example, Lu et al. [8] reported that CeO_2 nanorods exhibited a photovoltaic effect upon visible light illumination ($\lambda \geqslant 390$ nm). Zheng et al. [9] demonstrated that CeO_2 nanowires have better catalytic properties for CH_4 oxidation than commercial CeO_2.

So far, preparation of CeO_2 nanostructures is by no means a new research subject, however, much more effort is still needed to synthesize nano-CeO_2 with controllable morphology-, size-, and composition, and therefore the inherited excellent physical and chemical properties that are hard to achieve in their bulk counterparties [10]. Among numerous growth methods including microwave-hydrothermal method [11], a low temperature hydrothermal process has been proven to be a simple and cost-effective approach for the preparation of CeO_2 nanostructured materials. The use of mixed solvent system is a new preparation route, in which the addition of low-dielectric medium to the aqueous solution alters the thermodynamics of chemical reaction and kinetics of nucleation [12,13]. In this work, we report on the fabrication of morphology-controlled CeO_2 nanostructures with unique optical properties via a facile hydrothermal route. The structure and properties were characterized by various techniques, including X-ray photoelectron spectroscopy (XPS), scanning electron microscopy (SEM), high resolution transmission electron microscope (HRTEM), X-ray diffraction (XRD), Raman scattering, and photoluminescence (PL) spectra. Interestingly, thin CeO_2 nanorods, short-thick nanorods, and nanoparticles could be obtained by controlling the ethanol/water ratio in the ethanol–water solvent system. Exhilaratingly, the as-synthesized CeO_2 nanoparticles exhibited a remarkable near UV PL, which is mainly attributed to the abundant defect state between Ce 4f and O 2p bands, better crystallinity, and higher concentration of Ce^{3+} ions in the nanoparticles. The possible synthetic mechanism of morphology-controlled CeO_2 nanostructures was discussed in terms of the influences of hydrocarbon chains, dielectric constant, and viscosity of the solution on the thermodynamics of the reaction system and kinetics of nucleation.

* Corresponding author. Address: School of Physics and Materials Science, Anhui University, 111 Jiulong Road, Hefei 230601, PR China. Tel.: +86 551 5108049; fax: +86 551 5107237.
E-mail address: mrmeng@ahu.edu.cn (F. Meng).

0925-8388/$ - see front matter © 2013 Elsevier B.V. All rights reserved.
http://dx.doi.org/10.1016/j.jallcom.2012.12.096

2. Experimental details

2.1. Material preparation

All the reagents were of analytical grade purity and used as received without further purification. Four kinds of CeO_2 nanostructures, respectively referred to as A, B, C, and D, were synthesized by changing the volume ratio of ethanol to water. The growth of sample A was performed by dissolving 1.4903 g (4 mmol) $CeCl_3{\cdot}7H_2O$ in 20 mL distilled water with magnetic stirring, followed by the addition of 6 mL ethylenediamine under vigorous stirring for another 20 min, forming a homogeneous solution. Then 4 mL $N_2H_4{\cdot}H_2O$ (85%) was added dropwise to the obtained solution under continuous stirring for 15 min. The mixed solution was transferred into a 50 mL Teflon–lined autoclave and heated at 180 °C for 8 h. After the autoclave was naturally cooled to room temperature, the precipitate was collected by centrifugation, washed three times with distilled water and ethanol, and then dried in air at 80 °C for 10 h. The samples B, C, and D were synthesized by keeping the same parameters as same A except for using 20 mL mixed ethanol/water instead of pure water. The volume ratio of ethanol to water was 1:3, 3:1, and 1:0 respectively for samples B, C, and D.

2.2. Characterization

The crystal phases of CeO_2 nanostructures were analyzed by X-ray diffractometer (XRD, XD-3) with Cu Kα radiation. The morphology was examined by scanning electron microscope (SEM, S-4800, Japan) and transmission electron microscope (TEM, JEM-2100, Japan) equipped with an attached energy dispersive spectroscopy (EDS) system. The Raman spectra were recorded by a Raman spectrometer system (inVia-Reflex) using a laser with 532 nm excitation at room temperature. The chemical state was analyzed by X-ray photoelectron spectroscopy (XPS). Photoluminescence (PL) spectra were obtained by a fluorescence spectrophotometer (HORIBA FluoroMax-4P, HORIBA Jobin Yvon) using excitation light of 340 nm.

3. Results and discussion

3.1. Structure and morphology analysis

The phase purity of the as-synthesized nanostructures was examined by XRD measurements. Fig. 1 shows the XRD patterns of samples synthesized under different ethanol/water ratios. All the diffraction peaks from samples A, B, and C can be indexed to a fluorite cubic phase of CeO_2 (JCPDS 81-0792). They were found at 28.54°, 33.08°, 47.48°, 56.33°, 59.08°, 69.4°, 76.69°, 79.06°, and 88.41°, corresponding to ceria (111), (200), (220), (311), (222), (400), (331), (420), and (422) planes, respectively. No obvious sign of crystalline Ce_2O_3 or $Ce(OH)_3$ was detected by XRD, but for samples B and C two very weak peaks were indistinct found at 15.54° and 36.16°, which can be indexed to a hexagonal phase of $Ce(OH)_3$ (JCPDS 74-0665) with (100) and (111) planes, respectively. In addition, a considerable of Ce^{3+} ions was observed by XPS, as shown below, suggesting that the Ce^{3+} is distributed at the CeO_2 grain boundaries forming amorphous $Ce(OH)_3$ or Ce_2O_3.

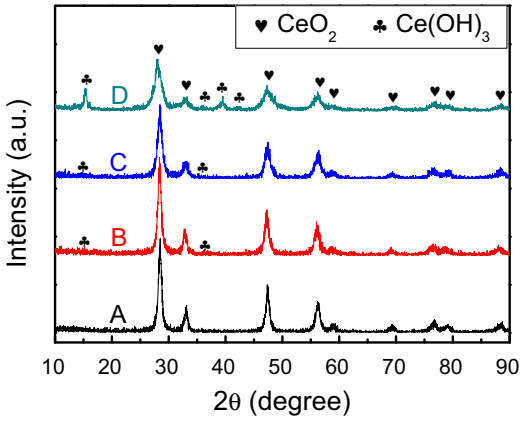

Fig. 1. XRD patterns of CeO_2 nanostructures synthesized in ethanol/water mixtures with the volume ratios of 0:1 (A), 1:3 (B), 3:1 (C), and 1:0 (D).

In addition to the diffraction peaks from the cubic ceria, however, the sample D showed extra peaks at 15.54°, 36.16°, 39.54°, and 42.42° which are respectively indexed to a hexagonal phase of $Ce(OH)_3$ (JCPDS 74-0665) with (100), (111), (201), and (210) planes, indicating that mixture of CeO_2 and its light hydroxide is synthesized using pure ethanol. The nanostructures synthesized in pure ethanol are significantly different from those obtained with ethanol/water mixtures.

Fig. 2 shows the SEM images of the as-synthesized nanostructures. It can be seen that CeO_2 thin nanorods of 15–30 nm in diameter and 100–300 nm in length were synthesized in water (sample A), while short-thick nanorods of 30–60 nm in diameter and 60–120 nm in length were synthesized in the 1:3 ethanol/water solvent. Continue to increase the ethanol/water ratio to 3:1, a mixture of short nanorods and nanoparticles was obtained. In pure ethanol, nanoparticles were formed. Obviously, the morphology of the as-synthesized nanostructures gradually changes from long nanorods to short ones, and then to nanoparticles with the increase of ethanol/water ratio in the growth solutions. There is a very small amount of nanoparticles observed in samples A and B. However, it is hard to see nanorods in sample D. It was demonstrated that the morphology of CeO_2 nanostructures is very sensitive to the volume ratio of ethanol to water, which can be used to control the nanostructure growth. The growth condition at a higher ethanol concentration is favorable for the formation of nanoparticles.

The influence of ethanol on the morphology of CeO_2 nanostructures may be attributed to three aspects as being discussed bellow. First, it is well known that hydrocarbon chains in ethanol may prevent electrostatic adsorption. As a result, the growth of long CeO_2 nanorods is restricted in the presence of ethanol, which leads a favorable condition for nanoparticle formation. Second, according to the classical Einstein–Strokes equation, $D = kT/6\pi\eta r$, the diffusion coefficient (D) of a solute of radius (r) in a solvent is in reciprocal proportion to the viscosity of the solution (η) [14,15]. It is well known that the η value of ethanol is bigger than that of water [16]. The addition of ethanol into water increases the viscosity of the solution and slows down the mass transfer, which is beneficial to the isotropic growth of nanoparticles. In our work, the sample synthesized in ethanol exhibited particle shape, which is consistent with the document [17]. Third, as is well known, the dielectric constant of ethanol is smaller than that of water, the addition of low dielectric medium ethanol to the aqueous solution not only alters the thermodynamics of the reaction system and the kinetics of nucleation, but also reduces the colloidal interactions of solid particles, as well as the interactions between particles and solvent, leading to different organization behaviors correlated with the delicate balance of attractions and repulsions [12]. The dielectric constant change with the increase of ethanol/water ratio is also favorable for the formation of nanoparticles due to the fact that ethanol/water mixtures with varied volume ratios possess different dielectric constant results in the difference in the solubility of the starting materials under supercritical conditions [17].

The as-synthesized nanostructures were analyzed by TEM and HRTEM as shown in Figs. 3 and 4. The TEM image in Fig. 3a shows that the CeO_2 nanostructures from sample B were mainly short-thick and uniform CeO_2 nanorods of 30–60 nm in diameter and 60–120 nm in length, which is consistent with the SEM observation. Fine nanoparticles with a diameter of 6–10 nm were also observed. Inset of Fig. 3a is a selected area electron diffraction (SAED) pattern obtained from one of the nanorods, indicating that the CeO_2 nanorods are polycrystalline materials. All the diffraction rings could be indexed to the cubic CeO_2 phase. Some defects can be seen from the HRTEM image (Fig. 3b), and as shown by white rectangle marked in and 3c. As shown in Fig. 3c, the ordered lattice can be seen clearly and the interplanar fringes are about 0.301 and 0.259 nm, representing the {111} and {200} lattice spacing of

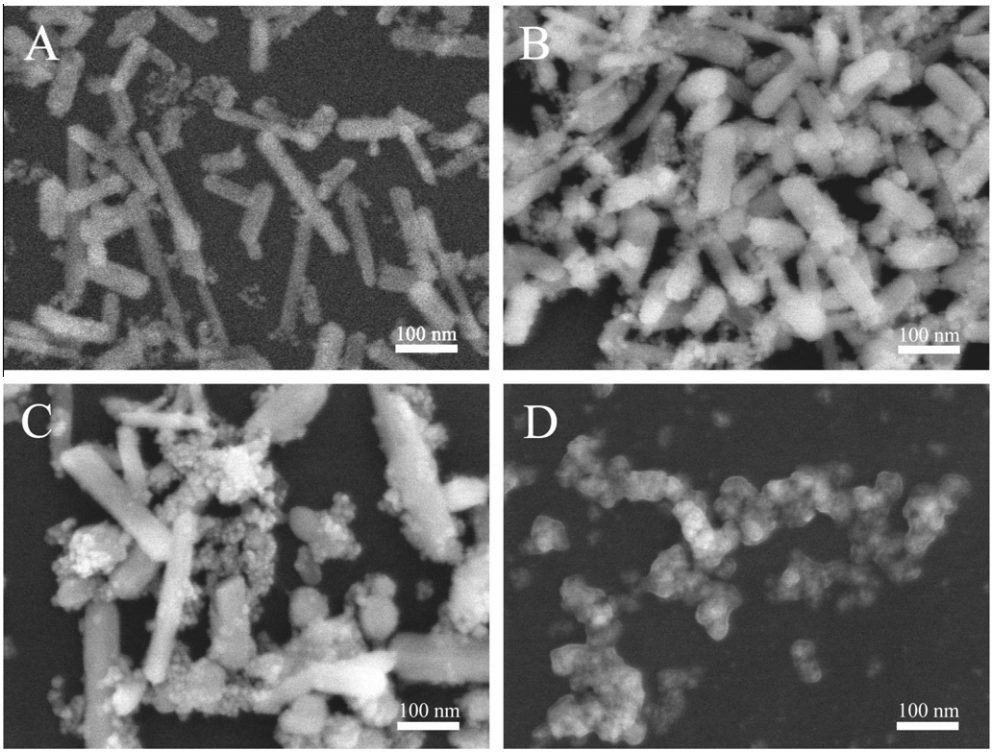

Fig. 2. SEM images of CeO_2 nanostructures synthesized in ethanol/water mixtures with the volume ratios of 0:1 (A), 1:3 (B), 3:1 (C), and 1:0 (D).

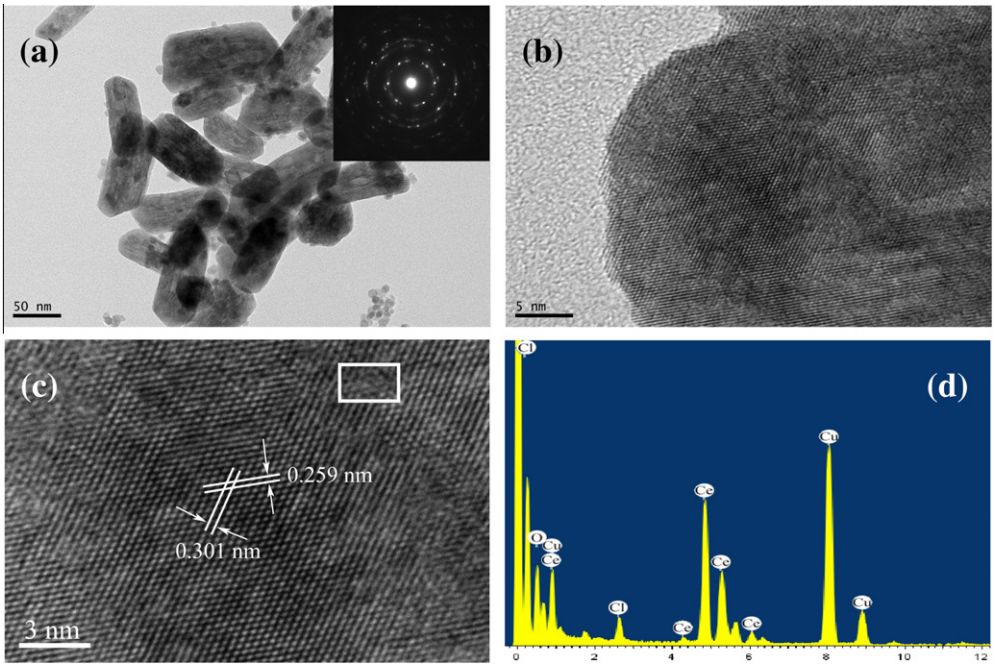

Fig. 3. (a) TEM image of CeO_2 nanorods synthesized in 1:3 ethanol/water mixture. Inset is the SAED pattern, and (b) HRTEM image, (c) the magnified image taken from the nanorod in (b), and (d) EDX spectrum of the nanorod shown in (b).

CeO_2, respectively. The EDX spectrum of Fig. 3d shows that both O and Ce were observed with an atomic ratio of O–Ce about 1.60. This low ratio suggests that Ce^{3+} ions may exist in the samples.

The TEM image in Fig. 4a was taken on sample D synthesized in ethanol without water. Homogeneous tiny nanoparticles were observed. The nanoparticles tend to aggregate together because of their large surface energy. The inset shows a SAED pattern taken from the agglomerated particles, which suggests that CeO_2 nanoparticles synthesized in ethanol have better crystallinity than the short nanorods in sample B. Fig. 4b shows the HRTEM image of a nanorod found in Fig. 4a. The fast Fourier transformation inserted in Fig. 4b further reveals the excellent crystallinity of the sample. The HRTEM of Fig. 4c confirms single-crystalline structure of the nanoparticles with crystallite size of 5–10 nm. The EDX spectrum

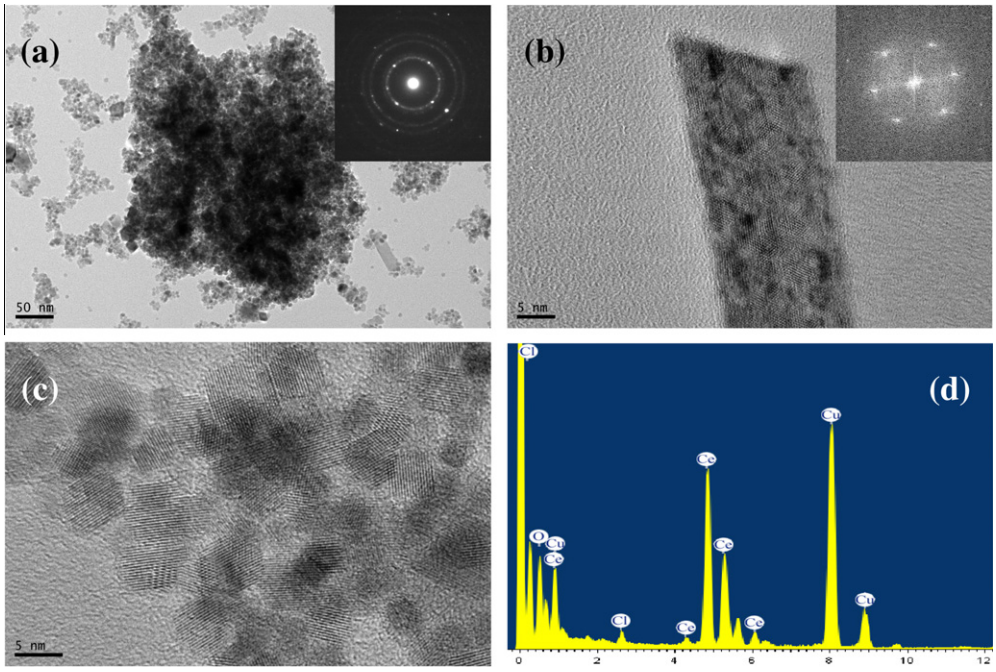

Fig. 4. (a) TEM image of CeO_2 nanoparticles synthesized in ethanol. Inset is an SAED pattern, and (b) HRTEM image of a nanorod found in (a). Inset is the fast Fourier transformation of the selected single nanorod revealing the excellent crystallinity, (c) HRTEM image of nanoparticles, and (d) EDX spectrum of the nanoparticles shown in (a).

shown in Fig. 4d produces an O/Ce ratio of 1.45, which is smaller than that of nanorods synthesized in the mixed solvents and suggests that there are likely more Ce^{3+} ions in the nanoparticles than the nanorods.

3.2. Composition and chemical state

Composition and chemical state of the as-synthesized nanostructures were studied by XPS. Fig. 5a and c shows the Ce 3d core levels from CeO_2 nanorods (sample B) and nanoparticles (sample D) respectively. The corresponding fitted deconvolutions of the Ce 3d levels are also included in Fig. 5. The u''' (916.99 eV), u'' (907.53 eV), u (900.03 eV), v''' (897.58 eV), v'' (888.43 eV), and v (881.85 eV) are attributed to Ce^{4+} ions, while u' (903.10 eV) and v' (883.99 eV) are the characteristic peaks of Ce^{3+} ions [18,19]. XPS integrated areas of individual peaks of the Ce 3d and O1s spectra of CeO_2 nanorods and nanoparticles are listed in Table 1. A semiquantitative analysis of the integrated peak areas can provide the concentrations of Ce^{3+} and Ce^{4+} ions in the synthesized CeO_2 nanorods and nanoparticles, as listed in Table 2, by using the following equations,

$$[Ce^{3+}] = \frac{A_{u'} + A_{v'}}{A_{u'''} + A_{u''} + A_{u'} + A_u + A_{v'''} + A_{v''} + A_{v'} + A_v} \quad (1)$$

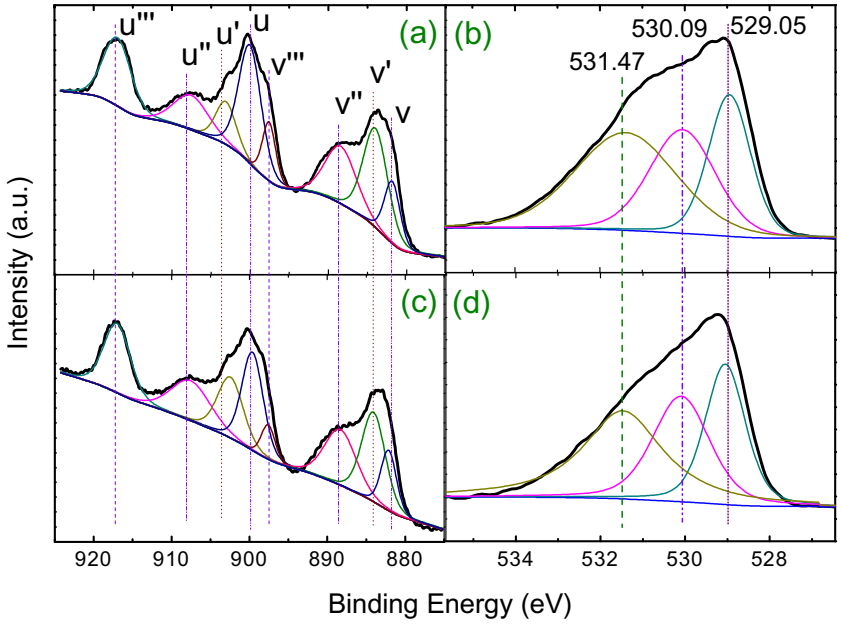

Fig. 5. XPS core level spectra of Ce 3d (a, and c) and O1s (b, and d) taken on CeO_2 nanorods and nanoparticles synthesized in ethanol/water mixtures with the volume ratio of 1:3 and 1:0, respectively.

Table 1
Integrated areas of individual XPS peaks of the Ce 3d and O1s from CeO_2 nanorods synthesized in ethanol/water mixture with the volume ratio of 1:3 (sample B) and nanoparticles synthesized in ethanol (sample D).

Samples	Ce ($3d_{3/2}$)				Ce ($3d_{5/2}$)					O1s	
	u'''	u''	u'	u	v'''	v''	v'	v	Ce^{4+}–O	Absorbed oxygen	Ce^{3+}–O
B	111064.8	70926.6	50793.8	156747.7	46026.1	104615.6	142833.2	57857.5	43383.46	49606.94	71530.67
D	109349.9	94036.2	92649.3	125192.3	28211.6	104783.7	126644.7	55934.2	43807.69	47115.78	66158.82

Table 2
Concentrations of Ce^{3+} and Ce^{4+} ions and stoichiometry x = [O]/[Ce] of CeO_2 nanorods synthesized in ethanol/water mixture with a volume ratio of 1:3 (sample B) and nanoparticles synthesized in ethanol (sample D).

Samples	[Ce^{3+}]	[Ce^{4+}]	x = [O]/[Ce][a]	x' = [O_{1s}]/[Ce_{3d}][b]
B	0.261	0.739	1.870	1.614
D	0.298	0.702	1.851	1.553

[a] Using Eq. (3).
[b] Using Eq. (4).

$$[Ce^{4+}] = \frac{A_{u'''} + A_{u''} + A_u + A_{v'''} + A_{v''} + A_v}{A_{u'''} + A_{u''} + A_{u'} + A_u + A_{v'''} + A_{v''} + A_{v'} + A_v} \quad (2)$$

where A_i is the integrated area of peak "i".

The Ce^{3+} ions can be distributed either in regions of sesquioxide Ce_2O_3 [20] or around oxygen-vacancy in CeO_2 [21]. In order to determine whether Ce^{3+} ions are associated with Ce_2O_3 or oxygen-vacancies, we calculated the oxygen content in the samples assuming that the total oxygen content is the sum of the required O to fully oxidize $Ce^{4+}$and Ce^{3+} to form CeO_2 and Ce_2O_3, respectively. Then taking into account the differences in stoichiometry x = [O]/[Ce] in CeO_2 (x = 2) and in Ce_2O_3, (x = 1.5), the ratio of O to the total Ce ions (Ce^{4+} + Ce^{3+}) is determined by using the amount of Ce^{4+} and Ce^{3+} ions as listed in Table 2 and the following equation,

$$x = \frac{[O]}{[Ce]} = \frac{3}{2} \times [Ce^{3+}] + 2 \times [Ce^{4+}] \quad (3)$$

Fig. 5b and d shows the O1s core levels for CeO_2 nanorods and nanoparticles, respectively, and also show the fitted deconvolutions of the O1s levels to the various states. It can be seen that the O1s spectra consist of three peaks at binding energy 529.05, 530.09, and 531.47 eV, which can be attributed to the absorbed oxygen [22], lattice oxygen in CeO_2 [23,24], and O related to the Ce^{3+} ions (Ce^{3+}–hydroxide and Ce^{3+}–oxide) [25,26]. The actual stoichiometry x' = [O]/[Ce] can be calculated directly from the XPS integrated areas of the O1s and Ce 3d peaks according to the following equation,

$$x' = \frac{O_{1s}}{Ce_{3d}} = \frac{A_O}{A_{Ce}} \cdot \frac{S_{Ce}}{S_O} \quad (4)$$

where A_O and A_{Ce} are the XPS integrated areas of the O1s and Ce 3d peaks, and S_{Ce} (=7.399) and S_O (=0.711) are sensitivity factors of Ce and O atoms respectively.

The existence of a considerable concentration of Ce^{3+} ions in both CeO_2 nanorods and nanoparticles was confirmed by the XPS data as summarized in Table 2. Moreover the concentration of Ce^{3+} ions in nanoparticles is higher than nanorods due to the complex reaction between Ce^{3+} ions and ethanol under alkaline condition according to,

$$Ce^{3+} + xOH^- + yC_2H_5OH \rightarrow [Ce(III)(OH)_x(C_2H_5OH)_y]^{\delta} \quad (5)$$

Therefore the increase of ethanol causes more Ce^{3+} ions to react with ethanol. As a result, the concentration of Ce^{3+} ions in nanoparticles is higher than nanorods. In addition, the actual stoichiometry (x') calculated by Eq. (4) is 0.2–0.3 smaller than that (x) calculated by Eq. (3), which suggests that two kinds of Ce^{3+} ions associated with Ce_2O_3 and oxygen vacancies in CeO_2 may coexist in the samples. From Table 2 it can also be seen that differentials between x and x' (i.e. x–x') increases with the increase of Ce^{3+} ions, which is in agreement with the literature [19] and implies that more oxygen vacancies in nanoparticles (sample D) may form as compared with CeO_2 nanorods (sample B).

3.3. Optical properties

To better understand the defects in the samples, Raman scattering was carried out and is shown in Fig. 6. One strong Raman peak centered at about 464 cm^{-1} dominates the spectra from all the samples. This peak originates from the F_{2g} Raman-active mode of CeO_2 cube structure [27–29], i.e. a symmetrical stretching mode of the Ce-8O vibrational unit [30,31]. Therefore, it should be very sensitive to any disorder in the oxygen sublattice resulting from thermal, doping, or grain-size induced effects [32]. The influence of the CeO_2 microstructures on the shape of the Raman spectra was observed by the broadening of the line and by the increase in its asymmetry due to the reduction of the phonon lifetime in the nanocrystalline regime [33]. The Raman line broadening of the CeO_2 nanostructures can be described by the dependence of the half-width, Γ, on the inverse of grain size, d_g, which follows a linear behavior as described below,

$$\Gamma(cm^{-1}) = 10 + \frac{124.7}{d_g} \quad (6)$$

The grain sizes calculated by Eq. (6) are 4.6, 5.2, 8.3, and 9.6 nm for the samples A, B, C, and D, respectively, indicating that the higher ethanol/water ratio resulted in larger crystallites in CeO_2 nanocrystals. This observation is consistent with our HRTEM measurements.

Raman peak positions obtained from Fig. 6 are 461.4, 461.4, 461.4, and 470.2 nm with corresponding peak line widths of 74,

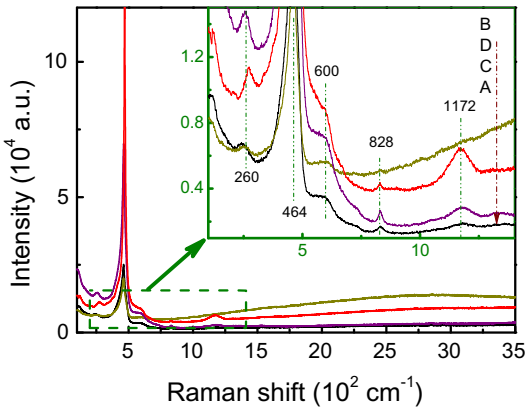

Fig. 6. Room temperature Raman spectra of CeO_2 nanostructures synthesized in ethanol/water mixtures with the volume ratios of 0:1 (A), 1:3 (B), 3:1 (C), and 1:0 (D). Inset is the magnified part as highlighted by the rectangle.

68, 50, and 46 cm^{-1} for samples A, B, C, and D, respectively. Several factors may have caused the changes in the main Raman peak position and line width, including phonon confinement, strain, broadening associated with the size distribution, defects, and variations in phonon relaxation with particle sizes [28]. It is likely that Ce^{3+} ions and oxygen vacancies in these samples are responsible for the changes in the Raman scattering as supported by the XPS and PL data.

The second-order features at 1172 cm^{-1} are very prominent in the samples D and C. But it is hard to see this peak for sample B. It can be attributed to the second-order Raman mode of surface superoxide species (O_2^-), and has little additional contributions from F_{2g} symmetry [27]. Moreover, the relative intensity of sample D at about 1172 cm^{-1} is obviously higher than other samples, implying the nanoparticles have more oxygen vacancies than other three samples. In fact the peak at about 1172 cm^{-1} is so broad and symmetrical that it makes no sense to assign it to a single critical point phonon overtone, rather, Weber et al. [27] simply assigned it to 2LO. The shoulder peak ranging from 560 to 600 cm^{-1} can be attributed to the presence of Ce^{3+} ions and oxygen vacancies [34]. The peak at about 828 cm^{-1} could be due to a second-order phonon, a local mode centered on vacancies, or the presence of another elemental species [28]. The peak near 260 cm^{-1} can be attributed to disorder in the system [32].

CeO_2 is a wide band gap semiconductor, whose Ce 4f energy levels localize at the forbidden band and lie about 3 eV above the valence band (O 2p) with width of 1.2 eV [35–37]. Its defect levels localized between the Ce 4f band and O 2p band can lead to wider emission bands. Fig. 7 shows the room temperature PL spectra of CeO_2 nanostructures synthesized under different ethanol/water ratios. Numerous emission peaks located at ~373, 383, 400, 420, 439, 450, 462, 468, 472, 482, 492, 542, and 564 nm are observed. These emission peaks between 400 and 500 nm form a broad emission band. Their PL intensities are slightly different from each other but the main emission peak maintains at 468 nm for samples A, B, and C. However, the PL spectrum of sample D is characterized with a wider and strong UV–violet–blue emission band ranging from 370 to 500 nm and a peak position at 406 nm instead of 468 nm as observed in the other samples. This is a very interesting and novel phenomenon. Maensiri et al. [30] reported the dependence of PL blue-shift on calcining temperature. From Fig. 7, it can be also seen that the peak intensity decreases with the increase of ethanol/water ratio from 0:1 up to 3:1 and then increases.

The strong broad UV–violet–blue emission band ranging from 370 to 500 nm of sample D may be understood as below. First, it may originate from the defect state existing extensively between the Ce 4f band and O 2p band [38,29]. The emission peaks located between 370 and 440 nm can be attributed to excitonic recombination corresponding to the near-band-edge emission of CeO_2 [39–41] and can be partly certificated by comparing the relationship of peak intensity and band gap. They are due to the 5d–4f transitions of Ce^{3+} between the ^2D ($5d^1$) ground state and the $^2F_{5/2}$ ($4f^1$) state. The other emission peaks between 445 and 500 nm may be attributed to the transitions from different defect levels to O 2p band. Obviously, the UV–violet–blue emission band of sample D is related to abundant defects in the nanoparticles. Our XPS and Raman results have indicated that sample D (nanoparticles) possess high oxygen-vacancy level, which is helpful for fast oxygen transport. Second, this phenomenon should be attributed to better crystallinity of sample D compared to the other samples, which is in agreement with the XRD and HRTEM results as well as literature [28]. Third, Morshed et al. [42] reported that the strong emission at 400 nm has a major contribution from Ce_6O_{11} phase. Ce_6O_{11} also has a Ce/O ratio higher than CeO_2 and hence a presence of Ce^{3+} ions in the oxide. Verma et al. [43] reported that the peaks near 425 and 486 nm are characteristic of the Ce^{3+} emission in Ce_2O_3 lattice. Based on these discussions, the strong emission at 400 nm may be partially attributed by the presence of Ce^{3+} ions. The concentration of Ce^{3+} ions in sample D should be the highest among those samples, which resulted in the highest near UV emission.

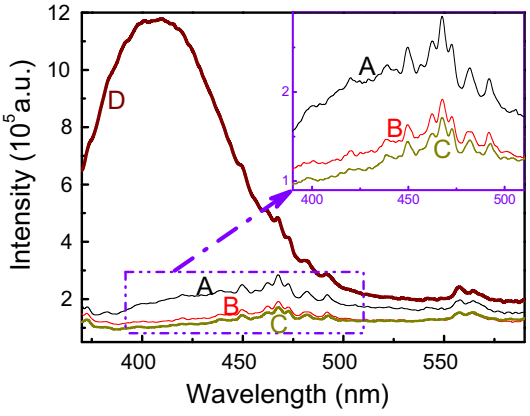

Fig. 7. PL spectra of CeO_2 nanostructures synthesized in ethanol/water mixtures with the volume ratios of 0:1 (A), 1:3 (B), 3:1 (C), and 1:0 (D). Inset is the magnified part as highlighted by the rectangle.

4. Conclusion

In summary, CeO_2 nanoparticles with a diameter of 5–10 nm were synthesized in ethanol by a facile hydrothermal method using $CeCl_3{\cdot}7H_2O$ as cerium source and $N_2H_4{\cdot}H_2O$ as mineralizer. Under similar hydrothermal conditions, use of water and 1:3 ethanol/water mixture as solvent resulted in the growth of CeO_2 nanorods of 15–30 nm in diameter and 100–300 nm in length, and short-thick nanorods of 30–60 nm in diameter and 60–120 nm in length, respectively. The effect of ethanol on the morphology of CeO_2 nanostructures can be mainly attributed to the influences of hydrocarbon chains, dielectric constant, and viscosity of the solution on the thermodynamics of the reaction system and kinetics of nucleation. The morphology change of the nanostructures has caused their optical properties significantly different. The CeO_2 nanoparticles showed a broad strong emission in the near UV which distinguished from those grown under different conditions. The unique UV–violet–blue emission of the nanoparticles may mainly originated from defect state existing extensively between the Ce 4f band and O 2p band, better crystallinity of the sample compared to those of other three samples, and higher concentration of Ce^{3+} ions in sample. The controllable morphologies, microstructures, and optical properties of CeO_2 should make the nanomaterials excellent candidates for applications in oxygen transportation, catalysts, fuel cells, ultraviolet blocks and luminescent materials.

Acknowledgments

This work was supported by the Scientific Research Foundation of Education Ministry of Anhui Province of China (Grant Nos. KJ2011A010 and KJ2012A029), and the Anhui Provincial Natural Science Foundation of China (Grant No. 1208085ME81).

References

[1] R. Si, Y.W. Zhang, L.P. You, C.H. Yan, J. Phys. Chem. B 110 (2006) 5994.
[2] H.R. Pouretedal, Z. Tofangsazi, M.H. Keshavarz, J. Alloys Compd. 513 (2012) 359.
[3] D.R. Ou, T. Mori, H. Togasaki, M. Takahashi, F. Ye, J. Drennan, Langmuir 27 (2011) 3859.
[4] H. Imagawa, A. Suda, K. Yamamura, S. Sun, J. Phys. Chem. C 115 (2011) 1740.

[5] S. Abdel-Hameed, F.H. Margha, M. Ouis, J. Alloys Compd. http://dx.doi.org/10.1016/j.jallcom.2012.11.132.
[6] D.M. Kempaiah, S. Yin, T. Sato, Cryst. Eng. Comm. 13 (2011) 741.
[7] L.W. Zeng, D.Q. Chen, F. Huang, A.P. Yang, L. Lei, Y.S. Wang, J. Alloys Compd. 534 (2012) 64.
[8] X. Lu, D. Zheng, P. Zhang, C. Liang, P. Liu, Y. Tong, Chem. Commun. 46 (2010) 7721.
[9] Y. Zheng, K. Liu, H. Qiao, Y. Zhang, Y. Song, M. Yang, Y. Huang, N. Guo, Y. Jia, H. You, Cryst. Eng. Comm. 13 (2011) 1786.
[10] M.G. Sujana, K.K. Chattopadyay, S. Anand, Appl. Surf. Sci. 254 (2008) 7405.
[11] R.C. Deus, M. Cilense, C.R. Foschini, M.A. Ramirez, E. Longo, A.Z. Simões, J. Alloys Compd. 550 (2013) 245.
[12] G. Chen, F. Zhu, X. Sun, S. Sun, R. Chen, Cryst. Eng. Comm. 13 (2011) 2904.
[13] C.S. Fang, Y.W. Chen, Mater. Chem. Phys. 78 (2003) 739.
[14] K. Kawasaki, Ann. Phys. 61 (1970) 1.
[15] P. Berge, M. Dubois, Phys. Rev. Lett. 27 (1971) 1125.
[16] E. Álvarez, Á. Cancela, R. Maceiras, J.M. Navaza, R. Táboas, J. Chem. Eng. Data 51 (2006) 940.
[17] M.K. Devaraju, S. Yin, T. Sato, Appl. Mater. Int. 1 (2009) 2694.
[18] S. Deshpande, S. Patil, S. VNT Kuchibhatla, S. Seal, Appl. Phys. Lett. 87 (2005) 133113.
[19] P. Patsalas, S. Logothetidis, Phys. Rev. B 68 (2003) 035104.
[20] N.V. Skorodumova, R. Ahuja, S.I. Simak, I.A. Abrikosov, B. Johansson, B.I. Lundqvist, Phys. Rev. B 64 (2001) 115108.
[21] F. Marabeli, P. Wachter, Phys. Rev. B 36 (1987) 1238.
[22] R. Yu, L. Yan, P. Zheng, J. Chen, X.R. Xing, J. Phys. Chem. C 112 (2008) 19896.
[23] A. Laachir, V. Perrichon, A. Badri, J. Lamotte, E. Chaterine, J.C. Lavalley, J. El-Fallah, L. Hilaire, F. le Normand, E. Quéméré, G.N. Sauvion, O. Touret, J. Chem. Soc. Faraday Trans. 87 (1991) 1601.
[24] A.E.C. Palmqvist, M. Wirde, U. Gelius, M. Muhammed, Nanostruct. Mater. 11 (1999) 995.
[25] G. Praline, B.E. Koel, R.L. Hance, H.I. Lee, J.M. White, J. Electron. Spectrosc. Relat. Phenom. 21 (1980) 17.
[26] A. Pfau, K.D. Schierbaum, Surf. Sci. 321 (1994) 71.
[27] W.H. Weber, K.C. Hass, J.R. Mabride, Phys. Rev. B 48 (1993) 178.
[28] J.E. Spanier, R.D. Robinson, F. Zhang, S.W. Chan, I.P. Herman, Phys. Rev. B 64 (2001) 245407.
[29] X.H. Lu, X. Huang, S.L. Xie, D.Z. Zheng, Z.Q. Liu, C.L. Liang, Y.X. Tong, Langmuir 26 (2010) 7569.
[30] S. Maensiri, C. Masingboon, P. Laokul, W. Jareonboon, V. Promarak, P.L. Anderson, S. Seraphin, Cryst. Growth Des. 7 (2007) 950.
[31] I. Kosacki, T. Suzuki, H.U. Anderson, P. Colomban, Solid State Ionics 149 (2002) 99.
[32] I. Kosacki, V. Petrovsky, H.U. Anderson, P.J. Colomban, Am. Ceram. Soc. 85 (2002) 2646.
[33] P. Parayanthal, F.H. Pollak, Phys. Rev. Lett. 52 (1984) 1822.
[34] J.R. Mabride, K.C. Hass, B.D. Poindexter, W.H. Weber, J. Appl. Phys. 76 (1994) 2435.
[35] C.A. Hogarth, Z.T. Al-Dhhan, Phys. Status Solidi B 137 (1986) K157.
[36] M. Niwano, S. Sata, T. Koide, T. Shidara, A. Fujimori, H. Fukutani, S. Shin, M. Ishigame, J. Phys. Soc. Japan 57 (1988) 1489.
[37] D.D. Koelling, A.M. Boring, J.H. Wood, Solid State Commun. 47 (1983) 227.
[38] A.H. Morhed, M.E. Moussa, S.M. Bedair, R. Leonard, S.X. Liu, N.A. El-Masry, Appl. Phys. Lett. 75 (1997) 2389.
[39] S. Gnanam, V. Rajendran, J. Sol–Gel Sci. Technol. 58 (2011) 62.
[40] Y.F. Huang, Y.B. Cai, D.K. Qiao, H. Liu, Particuology 9 (2011) 170.
[41] C.G. Kim, Appl. Phys. Lett. 79 (2001) 3047.
[42] A.H. Morhed, M.E. Moussa, S.M. Bedair, R. Leonard, S.X. Liu, N. El-Masry, Appl. Phys. Lett. 70 (1997) 1647.
[43] A. Verma, N. Karar, A.K. Bakhshi, H. Chander, S.M. Shivaprasad, S.A. Agnihotry, J. Nanopart. Res. 9 (2007) 317.